




Extrusion techniques on microstructure optimization and quantitative analysis of texture influence on ductility improvement for heat-resistant Mg–Nd–Zn–Zr magnesium alloy

J. He¹, W. Z. Chen^{1,2,*} , Z. J. Zhang¹, X. M. Chen¹, J. F. Ma¹, W. K. Wang^{1,2}, and W. C. Zhang^{1,2}

¹School of Materials Science and Engineering, Harbin Institute of Technology, Weihai 264209, People's Republic of China

²Weihai Lightweight Materials and Forming Engineering Research Center, Weihai 264209, People's Republic of China

Received: 13 September 2021

Accepted: 3 January 2022

Published online:
25 January 2022

© The Author(s), under exclusive licence to Springer Science+Business Media, LLC, part of Springer Nature 2022

ABSTRACT

Aiming at the ductility improvement of the rare-earth magnesium alloys, the influence of the microstructure refinement and texture on the strength and ductility was quantitatively analyzed for the Mg–Nd–Zn–Zr alloy subjected to the solid solution and extrusion. At an extrusion temperature of 500–150 °C for the solid-solute rods, abundant dynamic recrystallization and basal texture component change led to the generation of the alloy rods possessing an optimal ductility of 25–40% and a yield strength of 181–250 MPa. During the extrusion process, the <10–10>/ED deformed fiber texture was gradually formed, and the dynamic recrystallization led to a prominent microstructure refinement. The inclined basal texture emerged due to the preferential growth of the recrystallized grains. The yield strength varied significantly with the extrusion techniques, and its relationship with the grain size could be quantified by using the texture, characterized by the initial average equivalent basal Schmid factors \bar{m}_{bas} , influenced Hall–Petch relationship. The strengthening effect was included by the enhanced value of $\tau_{0,\text{bas}}$ (effective critical resolved shear stress based on basal slip) at yielding and the declined value of \bar{m}_{bas} from the strain hardening phenomenon during the low temperature extrusion. The high room-temperature ductility of 30–40% was dependent on the refined microstructure and weak inclined basal texture. The promotion of the uniform elongation from the inclined texture had a large contribution in the ductility improvement. This study reveals the regulating effect of the plastic processing on the strength and ductility (especially ductility), along with the importance of texture modification on the properties of the rare-earth heat-resistant magnesium alloys.

Handling Editor: Naiqin Zhao.

Address correspondence to E-mail: nclwens@hit.edu.cn

Introduction

The properties, such as high-temperature strength, excellent creep resistance, heat and corrosion resistance, etc., of the rare-earth (RE) magnesium alloys can meet the urgent need for the structural weight reduction in aerospace applications [1–3]. The rare-earth elements, such as Y, Gd, Nd, Sc, etc., are capable of inducing the solid solution strengthening effects in the magnesium matrix, along with excellent precipitation strengthening effects obtained through the aging heat treatment [4]. Among these, the Mg–Gd and Mg–Y heavy metal alloyed systems have attracted a significant attention owing to their outstanding age hardening and heat resistant properties, such as Mg–Gd–Y–Zr [5, 6], Mg–Gd–Zn–Zr [7, 8], Mg–Y–Nd–Gd [9], and Mg–Y–Zn [10, 11] (Table 1).

The strength of the Mg–Gd and Mg–Y alloys is enhanced after precipitation from the abundant second phases in the supersaturated solid solutions; however, the coarse grains produced after the solid solution treatment can lead to a poor ductility. For instance, Rong et al. [12] reported the ultimate tensile strength and yield strength of Mg–15Gd–1Zn–0.4Zr of 405 MPa and 288 MPa, respectively, after a solid solution treatment at 500 °C for 2 h and 520 °C for 12 h as well as aging at 200 °C for 65 h; however, the ductility was only 2.9%. The same scenario was reported by Zhang et al. [9] for the Mg–Y alloys, where the solid solution treatment at 525 °C for 6 h

and aging at 225 °C for 40 h for the cast Mg–4.3Y–3Nd–1.2Gd–0.2Zn–0.5Zr alloy led to the yield strength and ultimate tensile strength of 214 MPa and 316 MPa, respectively; however, the elongation was merely 4.4%. Also, Yu [15] reported only 8.3% elongation for the hot-extruded Mg–11.5Gd–4.5Y–1.5Zn–0.4Zr. In another study, Zhang [10] observed 11.0% elongation for the hot-extruded Mg–9Y–5Zn–0.6Zr.

The high content of the rare earth (> 8 wt%) elements can significantly enhance the cost of the alloys, thus inhibiting their application potential. Therefore, it is vital to focus on the development of the magnesium alloys with low alloy content (< 5 wt%) as well as remarkably enhanced ductility and formability [8, 11, 17–21]. The general mechanical properties of the mid/low RE magnesium after solid solution and hot extrusion are listed in Table 2. For instance, an improved ductility of 21.3% is noted for Mg–3.0Gd–2.7Zn–0.4Zr–0.1Mn after hot extrusion [8]. Nd, with the maximum solid solubility in magnesium of around 3.6 wt% and almost zero solid solubility (~ 0.08 wt%) at 200 °C, can exert a significant precipitation strengthening effect [22]. Generally, Mg–Nd alloy cannot be directly applied in the industry because of its large grain size as cast. To refine the grain size after casting, Zr is usually added as the nucleating agent [23]. At the same time, a small amount of Zn can further improve the aging peak strength and creep strength of Mg–1Nd–1Ce–Zr alloy [24]. Gavras reported that for Mg–Nd alloys, the addition of Zn can improve the tensile and

Table 1 Typical mechanical properties of high RE content (> 8 wt%) magnesium alloys

Composition	Heat treatment	Tensile properties			References
		UTS (MPa)	YS (MPa)	E (%)	
Mg–10Gd–3Y–Zr	525 °C × 10 h + 250 °C × 12 h	235	152	6.5	[5]
Mg–15Gd–1Zn–0.4Zr	500 °C × 2 h + 520 °C × 12 h + 200 °C × 65 h	405	288	2.9	[12]
Mg–15.6Gd–1.8Ag–0.4Zr	480 °C × 18 h + 500 °C × 8 h + 200 °C × 32 h	423	328	4.9	[13]
Mg–10Y–2.5Sm	540 °C × 6 h + 250 °C × 2 h	216	–	3.5	[14]
Mg–4.3Y–3Nd–1.2Gd–0.2Zn–0.5Zr	525 °C × 6 h + 225 °C × 40 h	316	214	4.4	[9]
Mg–11Y–5Gd–2Zn–0.5Zr	535 °C × 20 h + 225 °C × 24 h	307	240	1.4	[3]
Mg–15Gd–1Zn–0.4Zr	520 °C × 12 h + extruded at 490 °C (9:1)	423	359	10	[7]
Mg–10Gd–3Y–1.0Zn–0.5Zr	480 °C × 6 h + extruded at 400 °C (8:1)	347	231	11	[6]
Mg–11.5Gd–4.5Y–1.5Zn–0.4Zr	520 °C × 48 h + extruded at 420 °C (10:1)	453	387	8.3	[16]
Mg–9.5Y–3.5Zn–1Mn	450 °C × 18 h + extruded at 450 °C (10:1)	421	333	5.8	[17]
Mg–9Y–9Zn–0.6Zr	510 °C × 16 h + extruded at 400 °C (15:1)	351	245	11.0	[10]

Table 2 Typical mechanical properties of mid-low RE content (1–5 wt%) magnesium alloys

Composition	Heat treatment	Tensile properties			References
		UTS (MPa)	YS (MPa)	E (%)	
Mg–3.0Nd–0.4Zn–0.5Zr	530 °C × 8 h + 200 °C × 4 h	254	137	7.4	[18]
Mg–2.5Nd–0.6Zn–0.5Zr	515 °C × 16 h + 200 °C × 12 h	220	135	5.5	[19]
Mg–2.7Nd–0.6Zn–0.5Zr	530 °C × 14 h + 200 °C × 12 h	258	191	4.2	[20]
Mg–3.0Gd–2.7Zn–0.4Zr–0.1Mn	520 °C × 10 h + extruded at 350 °C (8:1)	341	315	21.3	[8]
Mg–3.5Sm–0.6Zn–0.5Zr	Extruded at 320 °C (7:1)	381	363	9.0	[21]
Mg–4Y–2Zn–0.5Al	450 °C × 2 h + extruded at 350 °C (20:1)	416	376	11	[11]

compressive properties at room temperature, during which a quasi-binary phase $Mg_3(Zn, Nd)$ and a ternary phase $Mg_{50}Nd_8Zn_{42}$ will be precipitated [25]. For instance, Zhang [26] reported the yield strength and ultimate tensile strength of 116 MPa and 198 MPa as well as an elongation of 14% for the Mg–3Nd–0.4Zn–0.4Zr alloy treated via direct chill casting. The hot rolling and heat treatment of the Mg–Nd alloys can effectively improve the tensile ductility at the ambient temperature by weakening the basal texture through recrystallization [27]. Therefore, the Mg–Nd–Zn-based system is commercially viable to develop the low-cost and high-strength RE magnesium alloys.

The plastic processing can effectively refine the microstructure and enhance the mechanical properties. Owing to the prominent brittleness at room and medium temperatures for the RE-enhanced magnesium alloys (Table 1), the plastic processing techniques to fabricate the high-strength heat-resistant magnesium alloys has not been paid a significant attention. Further, the microstructure control and property improvement based on the plastic processing technique are even more challenging, especially with the inevitable dispersive precipitation. This hinders the application of the high-strength heat-resistant magnesium alloys in the large-scale structural manufacturing applications. Therefore, the formability improvement via plastic forming is vital to modify the microstructure and properties.

Consequently, in this study, the extrusion process was adopted for the Mg–Nd–Zn–Zr alloy rods, and the solid solution-extrusion process was explored to analyze the influence of the plastic deformation on its structure. The room-temperature ductility improvement mechanism was quantitatively investigated so

as to provide a benchmark for designing the high-performance wrought magnesium alloy sheets suitable for a wide range of industrial applications.

Experimental

The commercial Mg–3.1 wt%Nd–0.4 wt%Zn–0.6 wt%Zr cast alloy was used as the raw material. The alloy was produced via the semi-continuous ingot casting. In order to fully achieve the ductility improvement during the solid solution treatment and subsequent aging strengthening effect, the solid solution at a temperature of 530 °C was used for a period of 1.5–24 h prior to extrusion. After 6 h, the rods were extruded in a 315 tons vertical extruder with a billet size of $\varnothing 50$ mm, the extrusion die size of $\varnothing 52$ mm, extrusion speed of 20–25 mm/s, and extrusion outlet diameters of 13 and 16 mm. The extrusion die was induction-heated at a constant temperature of 300 °C, and the temperature range of the billet was 150–500 °C. The temperature was determined at the extrusion outlet using an infrared thermometer with an error range of ± 10 °C. The graphite emulsion was used for the lubrication so as to obtain the extruded rods with an optimal surface quality. The process flow diagram is illustrated in Fig. 1.

The microstructure and texture in the ED-TD plane were identified using the electron backscattering diffraction (EBSD) analysis performed using a JEOL 733 electron probe equipped with the TSL OIM Analysis system. The Harmonic series expansion with a series rank of 16 and Gaussian half-width of 5° were used in OIM to generate the pole figures and calculate the corresponding maximal pole densities. The metallographic observations were performed

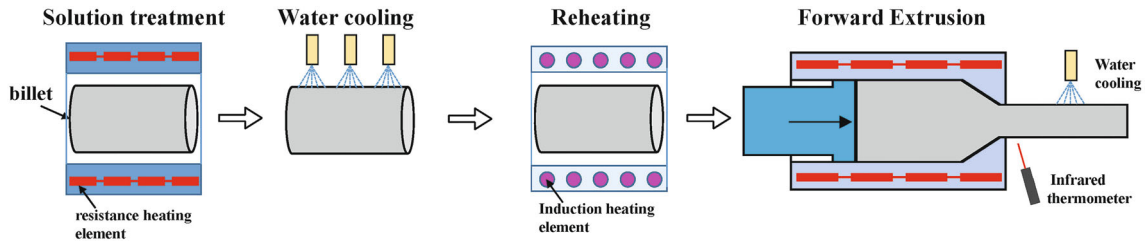


Figure 1 Schematic diagram of solid solution and hot extrusion process for the Mg–Nd–Zn–Zr alloy.

using a Hitachi S-570 scanning electron microscope (SEM), with the observation plane along the transverse and extrusion directions. The accelerating voltage was 20 kV for the EBSD and SEM analyses. The elemental analysis was conducted by the energy dispersive spectrometry (EDS) analysis at an accelerated voltage of 20 kV. The tensile tests were carried out at ambient temperature by employing INSTRON5569, with a constant speed equal to an initial strain rate of $6.7 \times 10^{-4} \text{ s}^{-1}$. The measurements were repeated thrice for accuracy. The dog-bone specimens with a gauge length of 15 mm and a diameter of 4 mm were machined out of the middle part of the as-extruded rods along the extrusion direction with a constant speed of 0.6 mm/min.

Results

Microstructural characteristics during solid solution treatment

Figure 2 displays the microstructure of the billet after solid solution treatment for 1.5, 3, 6, 9, 12, 15, 18, and 24 h as well as the second phase distribution observed by the SEM and EDS analyses. The as-cast Mg–Nd–Zn–Zr alloy was mainly composed of α -Mg, and the intergranular eutectic Mg_{12}Nd was distributed as the continuous network at the grain boundaries, occupying about 2.8% of the total area (Fig. 3). The aggregation at the grain boundaries was not conducive for coordinating the plastic deformation or exerting the aging precipitation strengthening effect. The SEM analysis of the solid solution treated structure revealed that the intergranular Mg_{12}Nd phases gradually decreased on enhancing the solution time from 9 to 18 h, followed by dissolution in the matrix with less than 0.1% area ratio. At the same time, a large number of dispersed round regions with

diameters of 10–40 μm appeared rapidly inside the grains, as shown in Fig. 4. The EDS analysis in Table 3 demonstrated that the spots distributed along the grain boundaries (Fig. 4a, point 1–4) were the Mg_{12}Nd accounting for 4.0–5.3% of the total area. A few Zr particles were also observed to form at the center of the enrichment zone. Fu et al. [28] reported the block-like and rod-like phases to be the ZrH_2 - and Zr-rich regions, respectively. As the solid solution time was extended to 24 h, the dispersed short block-like α -Nd phase with a length of $\sim 5 \mu\text{m}$ (Fig. 4b, point 6) reappeared within the grains, with the Nd content as high as 87.2% and area ratio of 0.8%.

In order to analyze the elemental diffusion and segregation, the solid solution treatment durations of 6 h and 24 h were selected to scan the elements, as shown in Fig. 5. After the solid solution treatment at 530 $^{\circ}\text{C}$ for 6 h, a considerable proportion of Nd in the alloy was still observed to be concentrated in the grain boundary in the form of Mg_{12}Nd . At the same time, a small amount of Zn was noted to segregate in the Nd-rich zone. The Zr element, which acted as a nucleating agent during solidification, was uniformly dispersed. After the solid solution treatment for 24 h, the Nd element in the matrix was re-accumulated and precipitated to form the α -Nd phase, which significantly reduced the solid solubility of the Nd element in the matrix. Such a high temperature accumulation and precipitation was not conducive to the improvement of the alloy strength after deformation. In summary, for the Mg–Nd–Zn–Zr alloys treated at 530 $^{\circ}\text{C}$ for 6 h, the intergranular Mg_{12}Nd phase still remained incompletely solute. A fully solid solution was achieved after 9–18 h, with the emergence of the round region Zr enrichment. On the other hand, after 24 h, an obvious α -Nd phase was noted to be supersaturated and segregated from the matrix.

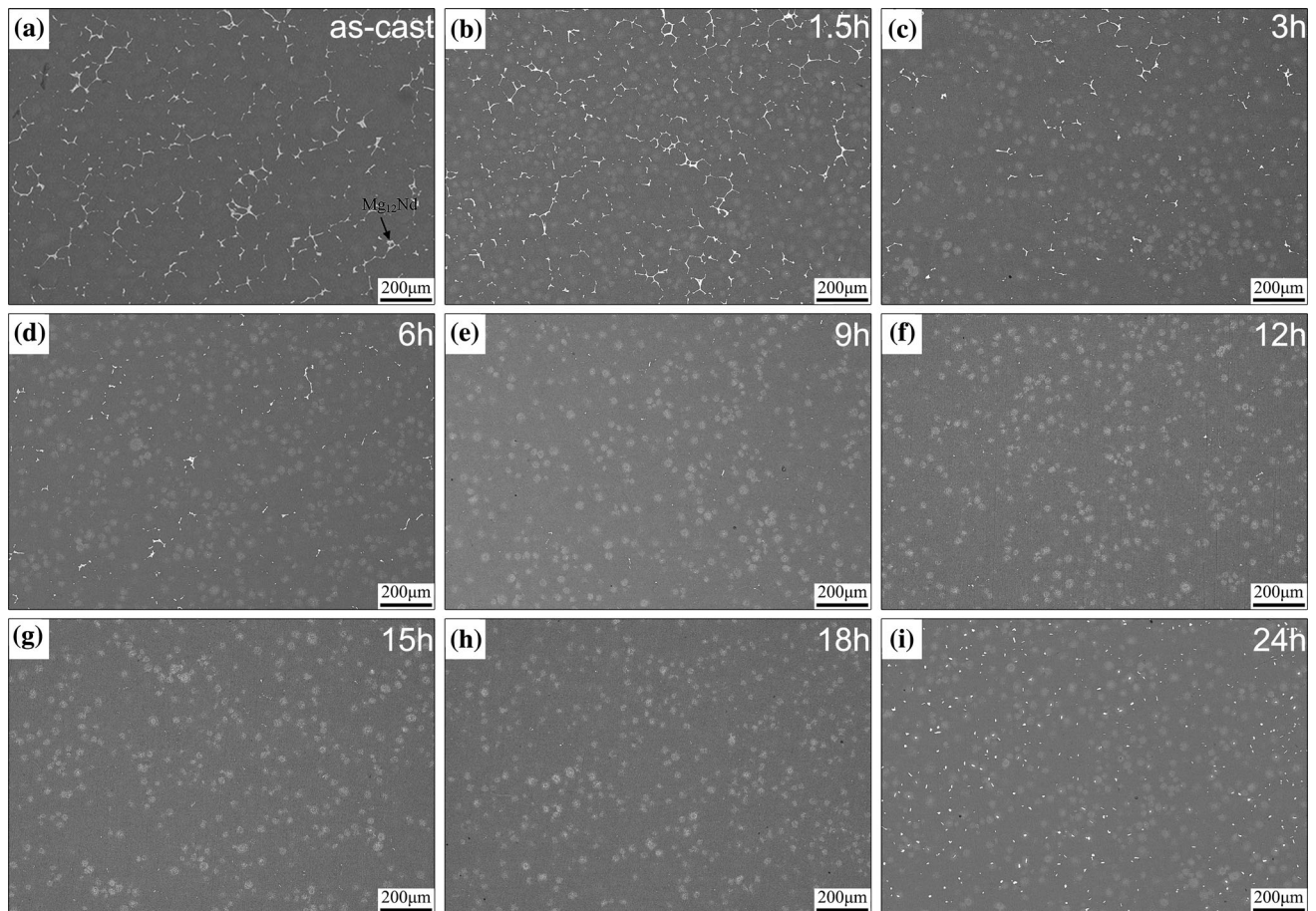


Figure 2 The SEM map of alloy after different solid solution time: **a** as-cast, **b** 1.5 h, **c** 3 h, **d** 6 h, **e** 9 h, **f** 12 h, **g** 15 h, **h** 18 h, **i** 24 h.

Microstructural characteristics after hot extrusion

The hot extrusion with varied extrusion temperatures and extrusion ratios was conducted at a fixed solid solution temperature of 530 °C for 9 h to explore the strength and ductility enhancement techniques. With an aim of enhancing the ductility, the hot extrusion process was carried out for the Mg–Nd–Zn–Zr alloy in the temperature range from 150 to 500 °C. The extrusion ratios of 16 and 10 were utilized to explore their impact on the microstructure.

Effect of extrusion parameters on the microstructural characteristics

A number of literature studies have suggested the significance of temperature in activating the deformation modes and microstructural characteristics [29–31]. For example, 0.5 T_m divides the boundary between the dynamic recovery and dynamic

recrystallization. In addition, for the dynamic recrystallization behavior, lowering the temperature can distinctly elevate the Zener–Hollomon parameter, refine the microstructure and enhance the mechanical properties [32, 33]. In this study, the extrusion temperature ranging from 150 to 500 °C was employed with an extrusion ratio of 16 for the Mg–Nd–Zn–Zr alloy, and the corresponding grain misorientation spread (GOS) microstructure characteristics are depicted in Fig. 6. GOS was determined by the average misorientation of each individual measurement point within the grain and represented the lattice distortion degree within the grains [32]. Referring to the literature [34] and grain morphology, the recrystallized grains were identified by the GOS values smaller than 2° (marked blue, green, and yellow), while the deformed grains elongated along the extrusion direction (ED) were greater than 2° and were marked red. The average area grain sizes were extracted from the maps and multiplied by 1.37 to convert them to the spatial average grain sizes. At an

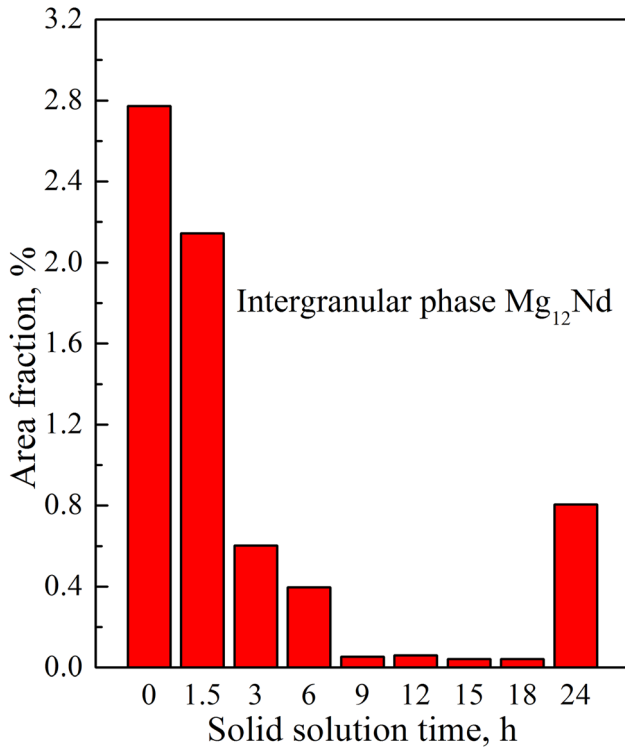


Figure 3 Percentage of intergranular second phase for Mg–Nd–Zn–Zr alloys under different solid solution time.

extrusion temperature of 500 °C, a typical completely dynamic recrystallized microstructure (with no deformed grains) emerged with an average grain size of 15.5 μm. At an extrusion temperature of 400 °C, the grains were further refined to an average size of 8.5 μm, along with a more equiaxed shape and a large quantity of grains satisfying the relation $GOS < 0.5^\circ$. The grain distribution turned into the lognormal fitting (Fig. 7) at a temperature of 400 °C. As temperature was decreased to 350 °C, a small amount of the deformed grains appeared, and the extent of the blue grains with $GOS < 0.5^\circ$ dramatically dropped from 0.81 to 0.27. Meanwhile, the

Figure 4 SEM map of Mg–Nd–Zn–Zr alloys under solid solution at 530 °C for **a** 6 h **b** 24 h. Points 1–4 in **a** were discontinuous $Mg_{12}Nd$, and points 5, 6 were Zr enrichment zone. Points 1–5 in **b** were Mg–Nd phase, and point 6 was Zr enrichment zone.

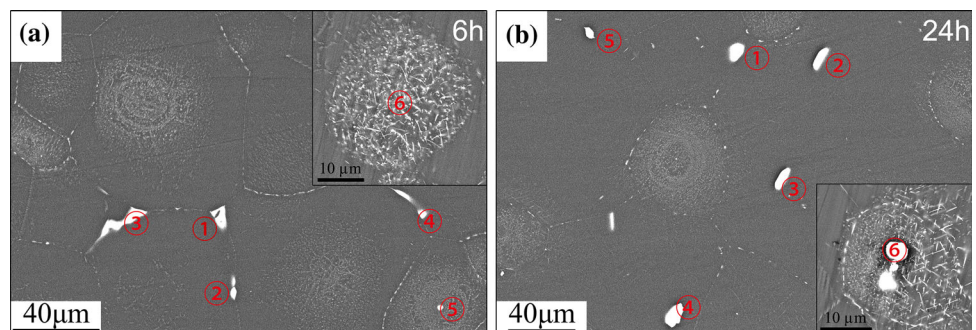


Table 3 EDS test for the second phase element for solid solute Mg–Nd–Zn–Zr alloys (at%)

6 h	Mg	Nd	Zn	Zr/at%	24 h	Mg	Nd	Zn	Zr/at%
1	94.5	4.8	0.7	0.0	1	85.8	13.8	0.3	0.1
2	94.0	5.2	0.8	0.0	2	39.7	58.3	1.0	1.0
3	95.5	4.0	0.8	0.0	3	12.9	84.3	1.2	1.6
4	94.1	5.3	0.6	0.0	4	9.0	87.3	1.7	2.0
5	77.2	0.4	0.3	22.1	5	74.7	24.1	0.6	0.6
6	73.3	0.5	0.4	25.8	6	12.1	0	0.7	87.2

average grain size continued to decline to 5.7 μm. At an extrusion temperature ranging between 300 and 250 °C, the grain size kept on decreasing to 4.0 μm, with no appearance of the deformed grains. However, the refining tendency ceased at a temperature of 150 °C with an average grain size increased to 5.9 μm. At this stage, the large deformed grains elongated along ED with a grain size of ~ 26 μm emerged, accounting for 13% of the total grains. Therefore, the extrusion temperature range of 200–400 °C was in accordance with the refined and fully dynamic recrystallized microstructure for the Mg–Nd–Zn–Zr alloy.

The microstructural variation with temperature at an extrusion ratio of 10 was also examined, and the results are presented in Fig. 8. During the whole extrusion process, the grains were refined more intensely, and the recrystallization degree was less incomplete as compared to the extrusion ratio of 16; however, the overall tendency was basically similar. It demonstrated the continuous refinement as the extrusion temperature decreased. Specifically, the extent of dynamic recrystallization was largely impaired as compared to the extrusion ratio of 16, with 12% deformed grains at 400 °C, 16% at 300 °C and 24% at 150 °C at an extrusion ratio of 10 in contrast with 0% deformed grains at 400 °C and

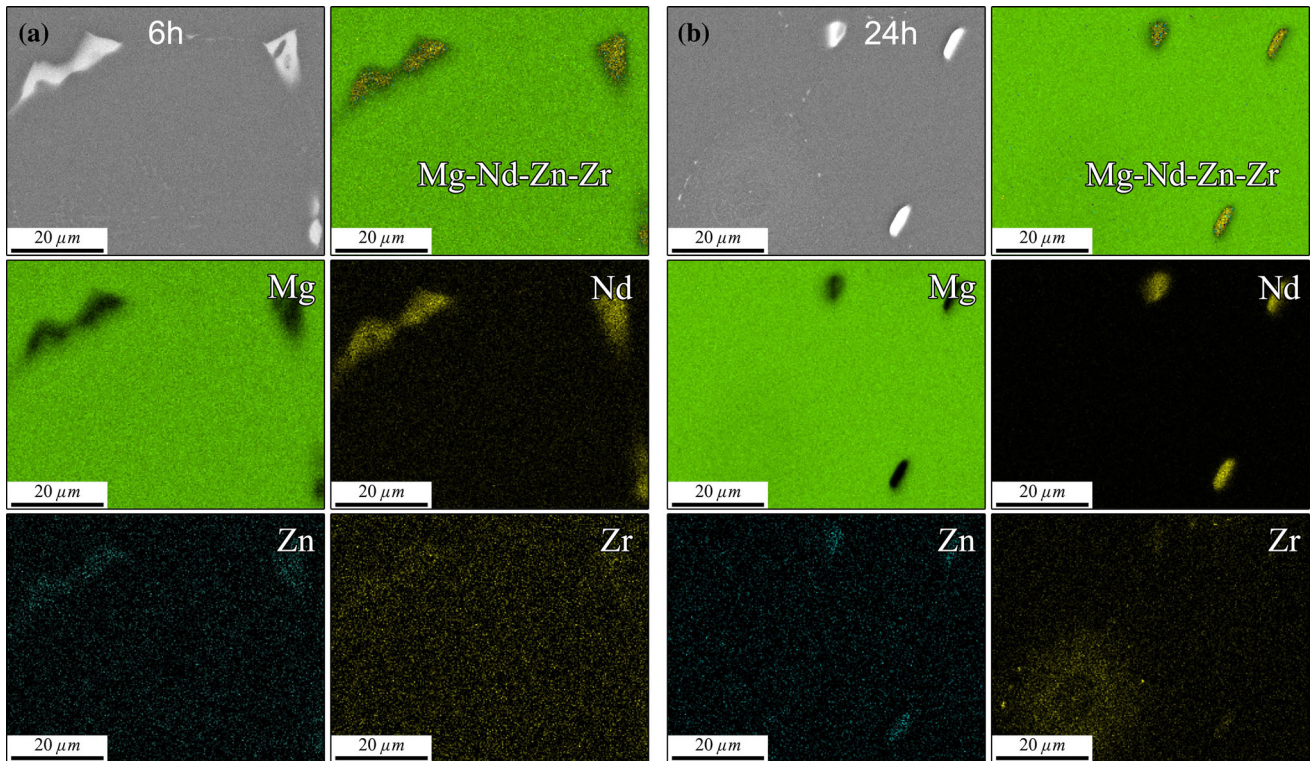


Figure 5 Element scanning of Mg–Nd–Zn–Zr alloy under solid solution at 530 °C for: **a** 6 h, **b** 24 h.

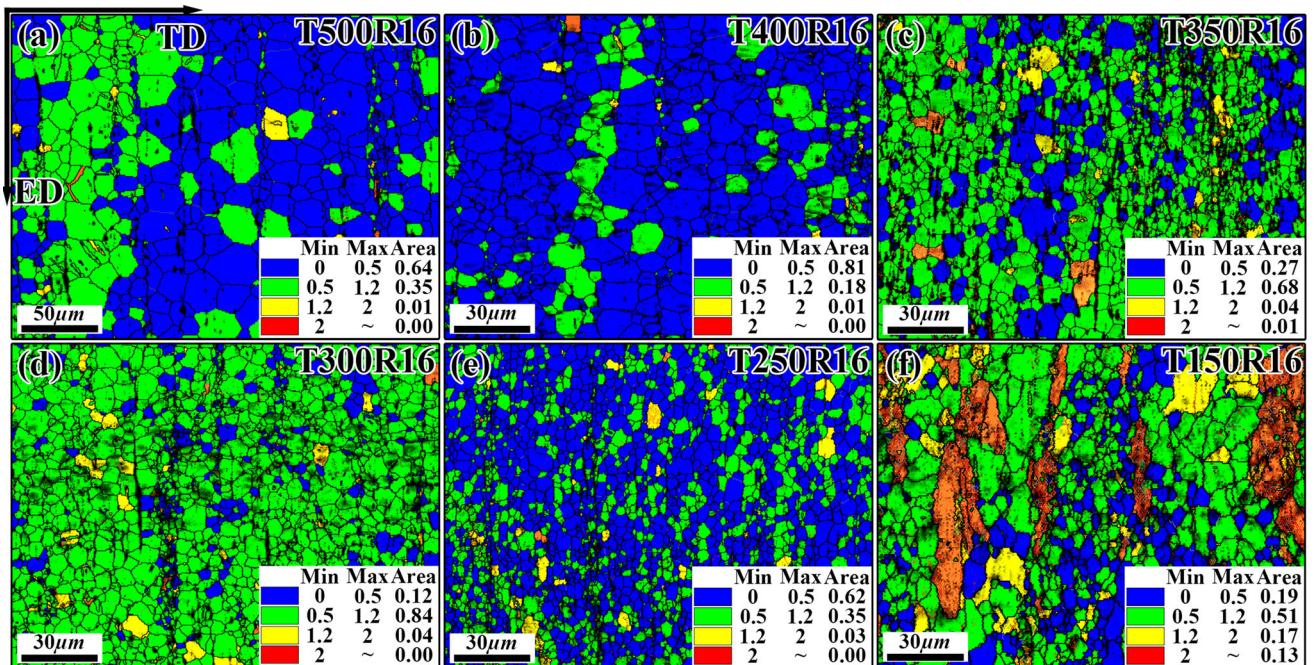


Figure 6 GOS map of extruded Mg–Nd–Zn–Zr alloys at extrusion ratio of 16 with different temperatures: **a** 500 **b** 400 **c** 350 **d** 300 **e** 250 **f** 150 °C.

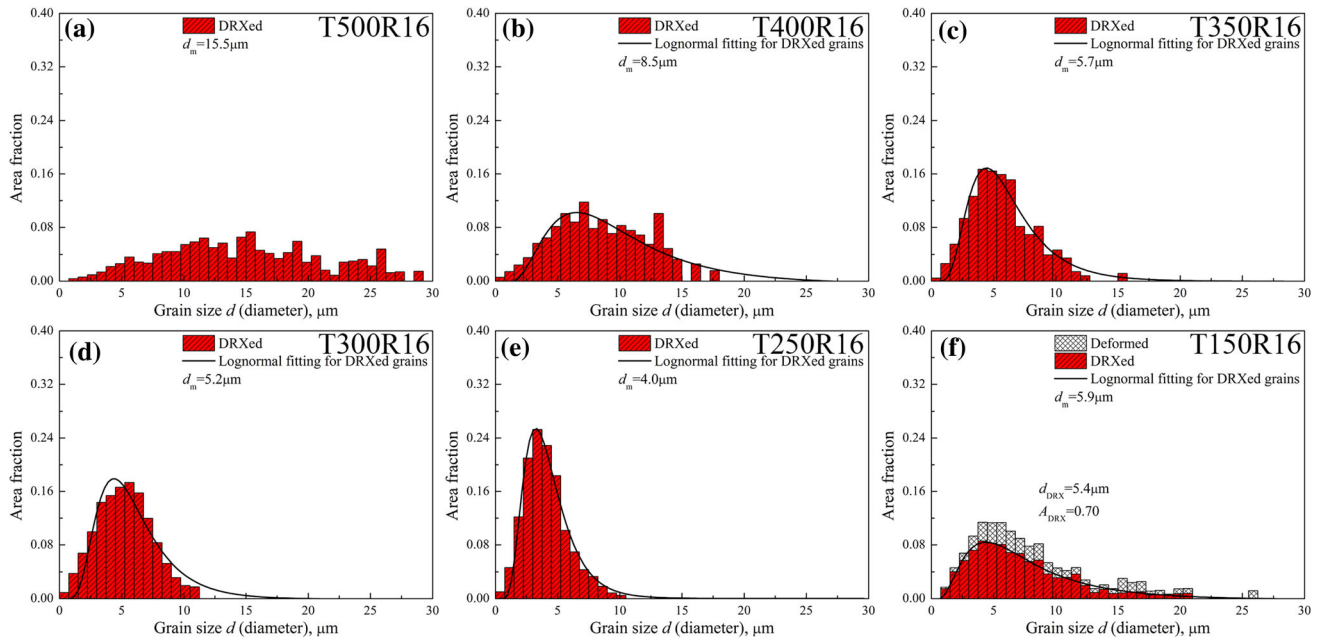


Figure 7 Grain size distribution for extruded Mg–Nd–Zn–Zr alloys at 500–150 °C with extrusion ratio of 16.

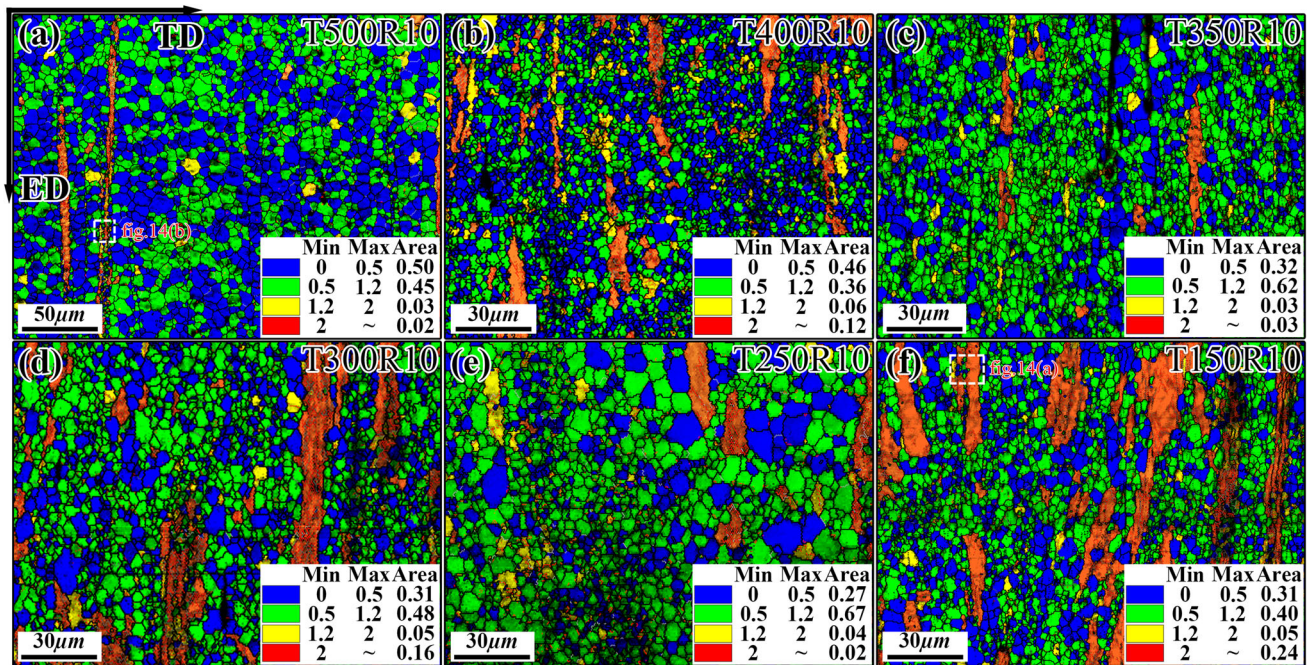


Figure 8 GOS map of Mg–Nd–Zn–Zr alloys after the hot extrusion with extrusion ratio of 10 and at temperature of: **a** 500 **b** 400 **c** 350 **d** 300 **e** 250 **f** 150 °C.

300 °C and 13% at 150 °C at an extrusion ratio of 16. The distinction was attributed to the high deformation heat and storage energy at high extrusion ratios, thus leading to enhanced dynamic recrystallization and less deformed structure. As for the grain sizes, the grains at an extrusion ratio of 10 were

significantly refined at every temperature as compared to the extrusion ratio of 16. Finally, at 150 °C, the average grain size was refined to 2.4 μm and 5.4 μm, as shown in Fig. 9, respectively. In conclusion, the extrusion ratio of 10 was more favorable for the grain refinement effect, leading to a small

recrystallization degree due to a small deformation heat, as compared to the extrusion ratio of 16.

Figure 10 demonstrates the TEM and EDS analyses of the alloy extruded at 250 °C at the extrusion ratios of 10 and 16. Further, Table 4 lists the elemental percentage in the second phase. For an extrusion ratio of 10, an abundant second phase with the grain size ranging from 0.1 to 0.4 μm and Nd element accounting for 6.4% were detected. The earlier observed Zr enrichment zone after the solid solution treatment disappeared with the extrusion and accounted for only 0.2% in the matrix. The composition of the second phase was identified in EDS as Mg_{12}Nd (point 1, 2, 3). At an extrusion ratio of 16, two morphologies of the second phase existed: the block shape of ~ 50 nm size (point 1, 2) and the rod shape of ~ 40 nm (point 3, 4) size. The EDS analysis revealed these phases to be Mg_{12}Nd and Mg-Nd-Zn , respectively. Compared with the second phase precipitation after the solid solution treatment, Mg_{12}Nd continued to exist; however, the Zr enrichment zones and $\alpha\text{-Nd}$ segregation were invisible after the hot extrusion.

Effect of extrusion parameters on texture

Figure 11 demonstrates the textural changes in the $\{0002\}$, $\{10-10\}$ and $\{11-22\}$ pole figures (PF) as well as the $[100]$ //ED inverse pole figures (IPF), as the

extrusion temperature decreased from 500 to 150 °C. In general, the texture of Mg–Nd–Zn–Zr after extrusion was completely different from the conventional extruded $\{0002\}$ //ED fiber in the RE-free magnesium alloys. After extrusion at 400 °C, the $\{0002\}$ basal plane almost deviated from ED and $\langle 0001 \rangle$, with a deflection angle of 75° (seen in its IPF), thus exhibiting a dispersed basal pole distribution. With the extrusion temperature declining to 250 °C, the scattered basal poles gradually concentrated to form the ring-shaped inclined texture with the $\{0002\}$ basal plane tilting 20°–60° from ED. Reflecting on the IPF, an obvious pyramidal $\{11-22\}$ – $\{10-11\}$ //ED fiber texture was observed to emerge. The maximum basal plane intensity stabilized around 2.8, and the maximum IPF intensity fluctuated mildly around 2.0. At a temperature of 150 °C, the $\{0002\}$ basal pole intensity moved closer to the center of the pole figure, thus illustrating that a large number of $\{0002\}$ basal planes were aligned with ED. In addition, a weak $\langle 10-10 \rangle$ //ED fiber texture component was present on the IPF, which did not appear previously. The extruded fiber texture component corresponded to the elongated deformed grains to rotate the lattices and less recrystallized grains to randomize the orientation in the GOS map.

The texture variations on decreasing the temperature at an extrusion ratio of 10 are illustrated in Fig. 12. The texture was overall stronger than the

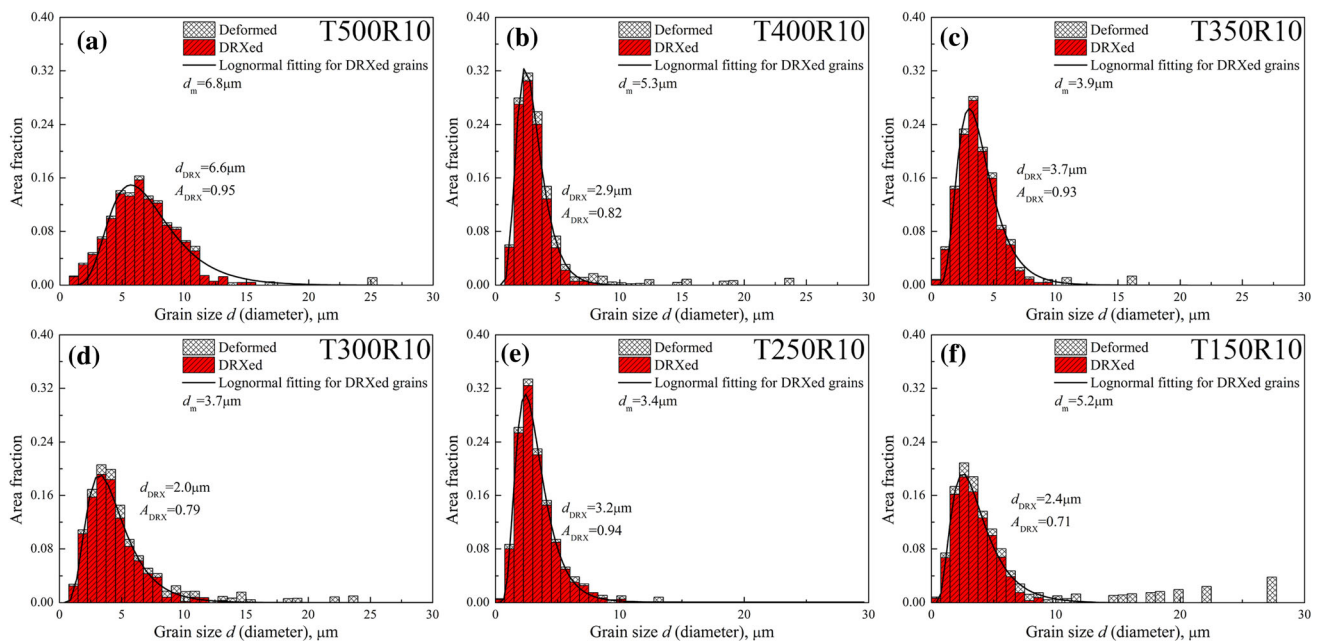


Figure 9 Grain size distribution for extruded Mg–Nd–Zn–Zr alloy at 500–150 °C with extrusion ratio of 10.

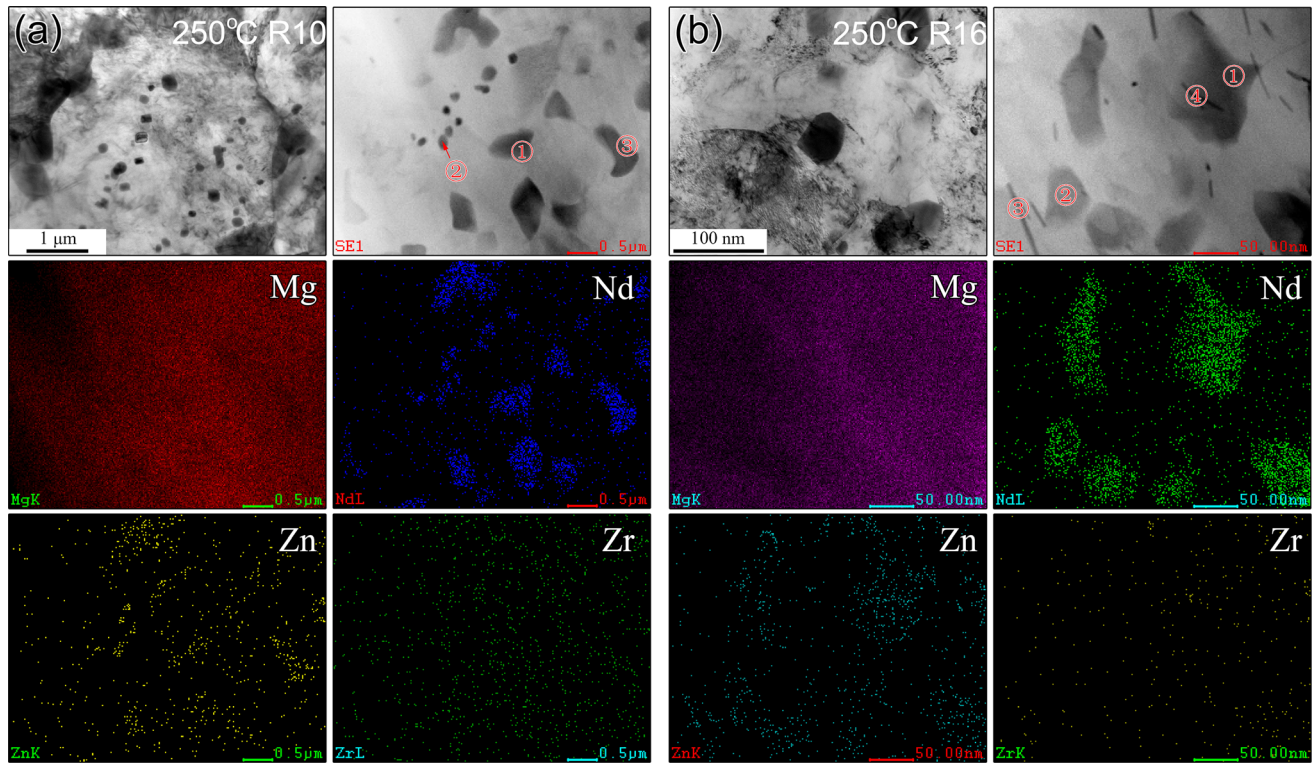


Figure 10 TEM and EDS figures for Mg–Nd–Zn–Zr alloy extruded at 250 °C with extrusion ratio of **a** 10, **b** 16. Points 1–3 in **a** were Mg₁₂Nd, and points 1, 2 in **b** were Mg₁₂Nd, and points 3, 4 were Mg–Nd–Zn.

Table 4 Element percentage in second phase for the Mg–Nd–Zn–Zr alloy extruded at 250 °C

R10	Mg	Nd	Zn	Zr/at%	R16	Mg	Nd	Zn	Zr/at%
1	93.0	6.4	0.4	0.2	1	92.4	7.2	0.4	0.0
2	93.0	5.4	0.9	0.7	2	90.5	8.9	0.6	0.0
3	89.0	10.0	0.9	0.1	3	89.9	8.8	1.2	0.1
					4	90.8	7.4	1.8	0.0

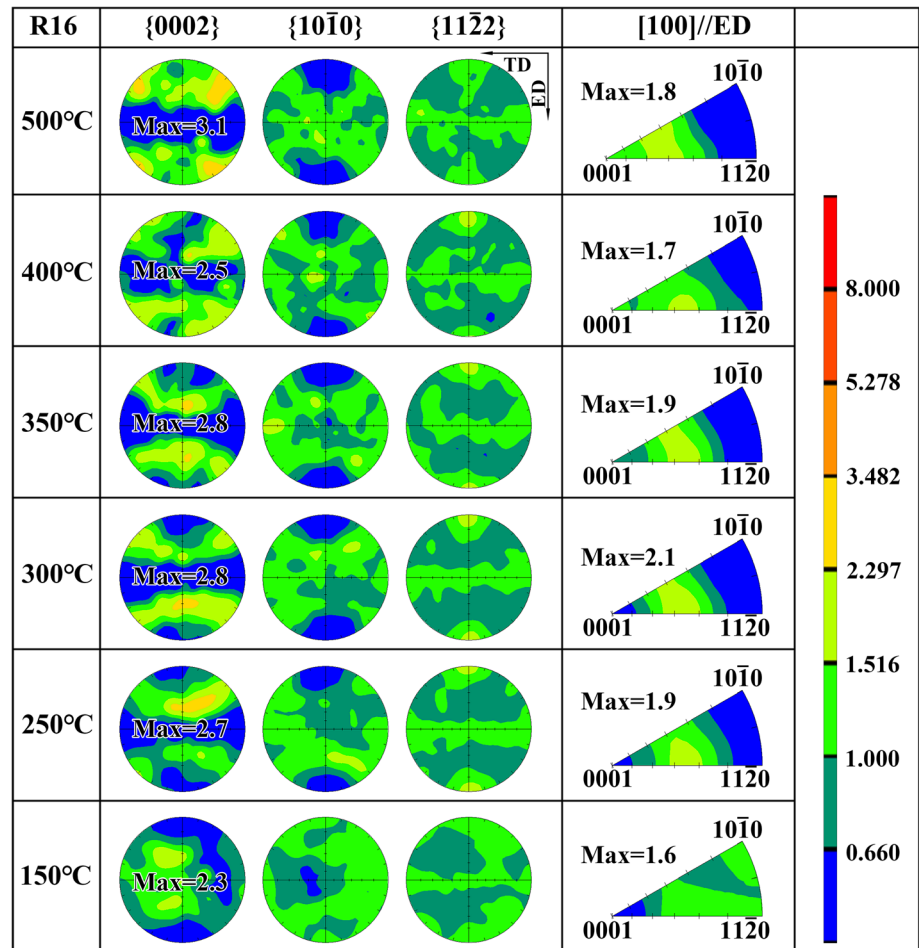
extrusion ratio of 16, with an appearance of a more concentrated {0002} <10–10> fiber texture component. At a temperature of 500 °C, a ring-shaped inclined texture was observed on the {0002} plane, the same as that in the low temperature part of the texture at an extrusion ratio of 16, and the ring width was around 45° (as shown in IPF). At a temperature of 400 °C, the <10–10> // ED fiber texture component emerged on IPF with a maximum intensity of 2.7, and intensity poles were distributed more densely on the equator plane in the {0002} pole figure. In the meantime, the inclined texture component was significantly weakened, demonstrating a more dispersed or light-shaded pattern on the IPF. The inclined texture

component disappeared eventually at a temperature of 150 °C, and a strong fiber texture with the maximum basal plane intensity of 5.6 was achieved. Associated with the microstructural characteristic, the less recrystallized grains due to the low deformation heat at a small extrusion ratio were incapable of sufficient reorientation to disperse the texture distribution. In the meanwhile, the existing large deformed grains maintained the initial extruded fiber texture so as to form a strong texture at an extrusion ratio of 10.

Mechanical properties of the extruded Mg–Nd–Zn–Zr alloy rods

Figure 13 and Table 5 depict the mechanical properties of the Mg–Nd–Zn–Zr rods extruded at different extrusion ratios and extrusion temperatures to analyze the effect on the mechanical properties. At the same extrusion ratio, the lower was the extrusion temperature, the superior were the mechanical properties. The Mg–Nd–Zn–Zr rods exhibited higher ductility and lower yield strengths at large extrusion ratios, but smaller ductility and higher yield strength

Figure 11 {0002}, {10–10}, and {11–22} pole figures and inverse pole figures for Mg–Nd–Zn–Zr alloy extruded at 500–150 °C with extrusion ratio of 16.



at small extrusion ratios. At the same extrusion temperature, the different extrusion ratios exerted an obvious impact on the yield strength and ductility of the extruded alloys. Specifically, at an extrusion ratio of 10, the lower was the extrusion temperature, the higher was the yield strength of the extruded rods. Among these, for the Mg–Nd–Zn–Zr rod extruded at 250 °C, the yield strength reached 250 MPa, whereas the ultimate tensile strength and fracture elongation were determined to be 278 MPa and 25% respectively. Afterwards, on increasing the extrusion temperature, the mechanical properties gradually decreased and reached the minimum. After extrusion at 400 °C, the yield strength and ultimate tensile strength were 195 MPa and 250 MPa; however, the fracture elongation was appreciable (36%). In comparison, the Mg–Nd–Zn–Zr alloys extruded at an extrusion ratio of 16 and a low extrusion temperature possessed high yield strength. For instance, for the Mg–Nd–Zn–Zr rods extruded at 250 °C, the yield strength and ultimate tensile strength were 181 MPa

and 247 MPa respectively, with a fracture elongation of 43%. In summary, for the Mg–Nd–Zn–Zr alloys, the ductility could reach between 25 and 40% after a single extrusion cycle, and the yield strength varied between 181 and 250 MPa, thus displaying an effective control of the ductility improvement. Based on the aforementioned microstructural observation, the difference in the mechanical properties could be attributed to the differences in the grain refinement, texture change and residual strain hardening influenced by the corresponding plastic processing.

Discussion

Microstructural evolution during the extrusion of the Mg–Nd–Zn–Zr rods

Comparing the texture of the Mg–Nd–Zn–Zr alloy after extrusion at 150 °C and 500 °C, it was revealed

Figure 12 {0002}, {10-10}, and {11-22} pole figures and inverse pole figures for Mg–Nd–Zn–Zr alloy extruded at 500–150 °C with extrusion ratio of 10.

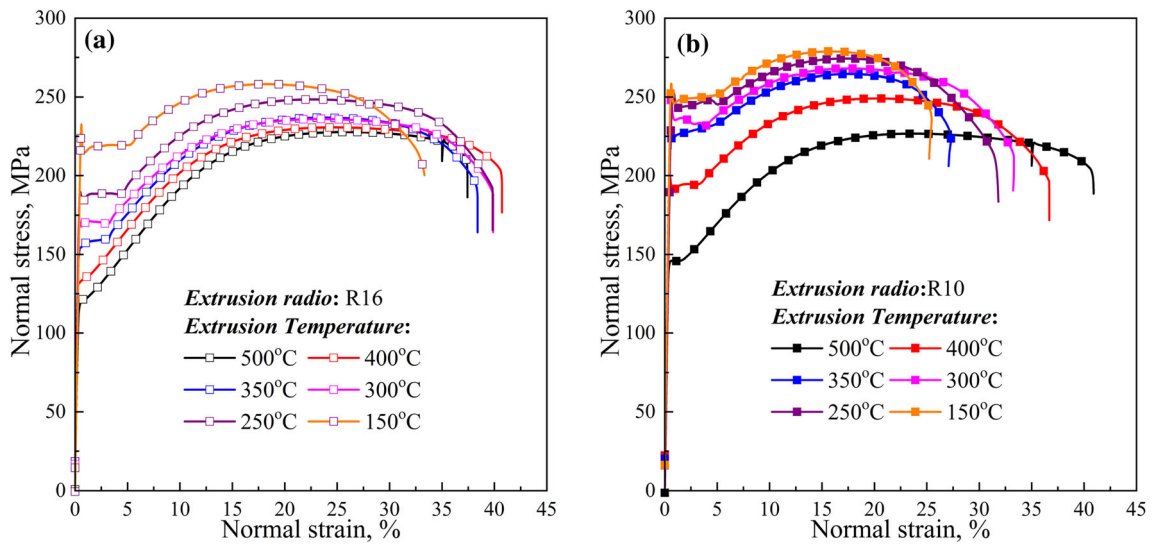
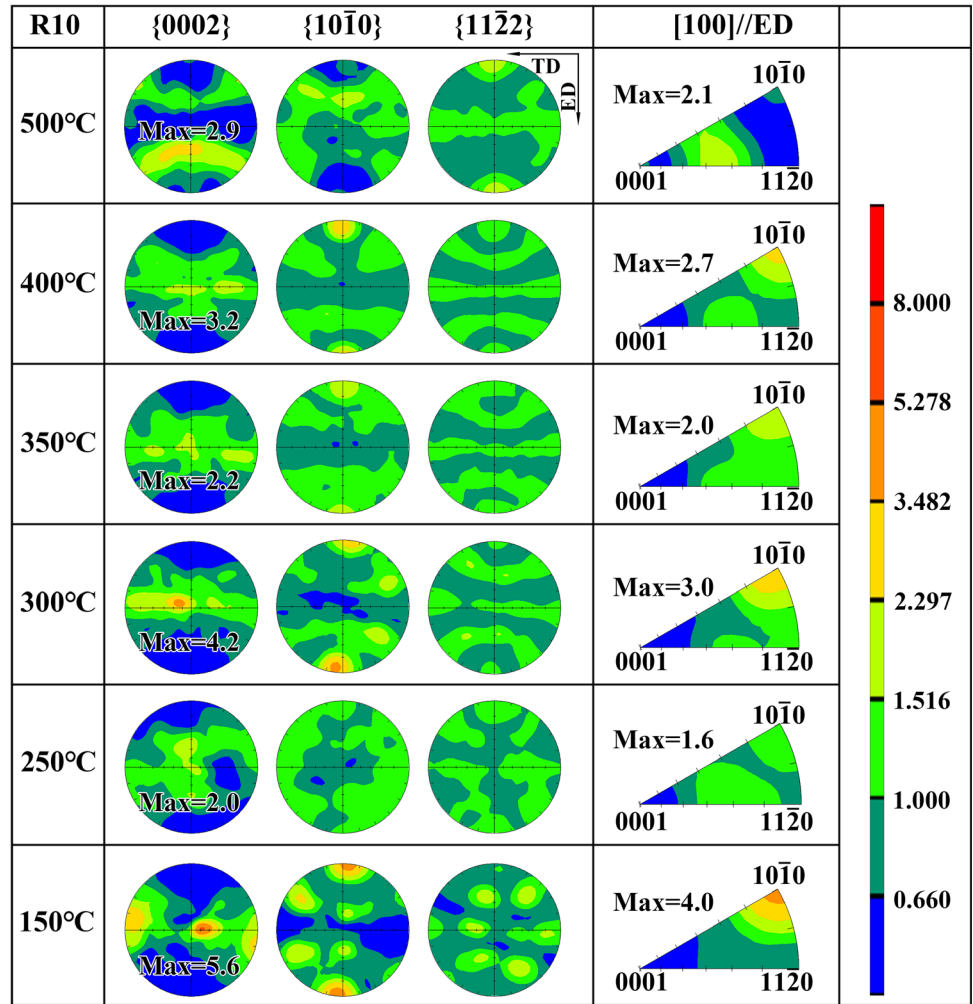


Figure 13 Room temperature stress–strain curves of Mg–Nd–Zn–Zr alloy extruded at 500–150 °C with extrusion ratio of a 16, b 10.

Table 5 Summarized mechanical properties of as-extruded Mg–Nd–Zn–Zr alloy rods

Condition	YS (MPa)		UTS (MPa)		UFE (%)		FE (%)	
	R16	R10	R16	R10	R16	R10	R16	R10
T500	116 ± 2	145 ± 8	226 ± 1	227 ± 8	26.0 ± 0.0	23.4 ± 1.6	37.5 ± 0.1	40.9 ± 1.2
T400	134 ± 2	195 ± 8	232 ± 1	249 ± 3	24.3 ± 0.1	20.2 ± 0.9	39.6 ± 1.1	36.7 ± 0.4
T350	151 ± 6	223 ± 2	234 ± 3	265 ± 2	24.1 ± 0.4	17.6 ± 0.7	39.4 ± 1.0	27.3 ± 2.2
T300	164 ± 4	243 ± 6	234 ± 2	268 ± 3	24.0 ± 0.7	17.3 ± 0.5	41.8 ± 1.9	33.3 ± 0.8
T250	184 ± 3	253 ± 2	248 ± 0	274 ± 2	21.9 ± 0.6	17.0 ± 0.1	38.2 ± 1.6	31.8 ± 1.7
T150	220 ± 1	250 ± 3	257 ± 1	279 ± 3	18.2 ± 0.1	15.8 ± 0.1	32.8 ± 0.5	25.5 ± 1.4

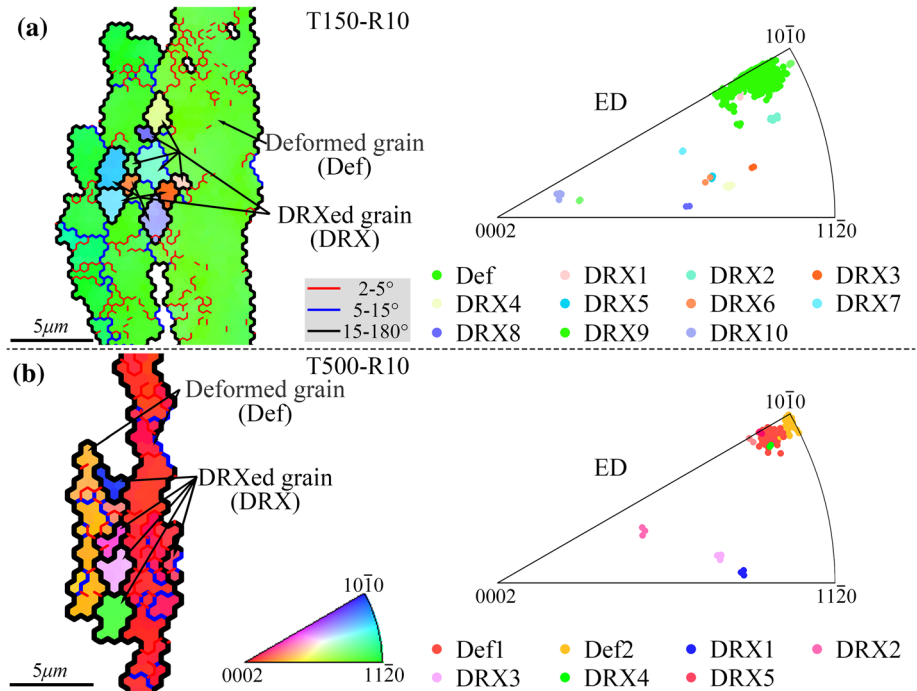
YS yield strength, UTS ultimate tensile strength, UFE uniform elongation, FE fracture elongation

that the deformed microstructure corresponded to the $\langle 10\text{--}10 \rangle // \text{ED}$ fiber texture component, which implied that the basal slip was still dominant for the rare-earth magnesium alloys deformed under 500 °C. The recrystallization grains in accordance with the inclined {0002} basal texture component stemmed from two mechanisms: preferential nucleation or preferential growth [35–37]. Taking a close look at the orientation between the matrix and refined recrystallization grains inside the deformed grains in Fig. 14, the refined recrystallized grains were observed to be oriented away from ED in the 15°–80° range. Specifically, at an extrusion temperature of 150 °C, the deflection angle in the map ranged from 15° to 80°. On the other hand, for an extrusion temperature of 500 °C, the recrystallized grains were oriented from 10° to 50°. This indicated that the recrystallization nucleation tended to weaken the texture by dispersing the pole points away from ED. This also meant that the inclined {0002} basal texture component was likely to result from the predominant preferential growth at the later extrusion stage and before the water quenching.

Combining the microstructural characteristics during the extrusion process, a predominant recrystallization occurred in the Mg–Nd–Zn–Zr alloy after extrusion in a large temperature range, resulting in a severe microstructure refinement with a grain size less than 5 μm. It was accompanied by the transition from the traditional strong basal texture. The microstructure evolution in the Mg–Nd–Zn–Zr alloy during the extrusion process could be explained as follows. The deformation distortion inside the grains continuously increased as the extrusion proceeded and gradually formed the typical $\langle 10\text{--}10 \rangle // \text{ED}$ fiber

deformation texture. As the distortion energy accumulated at some point, the dynamic recrystallization with the discontinuous nucleation occurred in the microstructure, thus resulting in a severe refinement of the microstructure. In addition, the orientation of the recrystallization grains was deviated from the matrix to weaken the basal texture. During the later extrusion stage, the deviated weakened recrystallization grains grew preferentially, and the texture gradually converted into the inclined {0002} recrystallized texture. At the end, the microstructure represented the combined outcome of the plastic deformation and recrystallization and was significantly influenced by the extrusion parameters. The influence mainly manifested in two aspects: the microstructure refinement by recrystallization and percentage of the recrystallized grains. The microstructure refinement was affected by the Zener–Hollomon [38, 39] value, which increased as the extrusion temperature declined. It resulted in a significant refinement of the recrystallized grains, thus obtaining the refined grains under 5 μm an extrusion temperature of 300 °C. Thus, a higher extrusion ratio attributed to a higher deformation heat, thereby increasing the actual temperature in the deformation zone. This implied that a low Zener value caused the coarsening of the microstructure at a large extrusion ratio. The percentage of the recrystallization grains was mainly dependent on the extrusion ratio, i.e., the plastic deformation degree. The higher was the extrusion ratio, the severer was the plastic deformation degree and the higher was the deformation temperature, thus contributing to the fully recrystallized microstructure and stable inclined {0002} basal texture. However, at the small extrusion ratios, for

Figure 14 The orientation of the deformed and dynamic recrystallized grains in extruded Mg–Nd–Zn–Zr alloy with extrusion ratio of 10 at a 150 °C, b 500 °C.



the extrusion temperature lower than 400 °C, the mixed microstructural characteristic of the deformed and recrystallized grains was observed. On decreasing the temperature, the percentage of the deformed microstructure was continually enhanced, and the microstructural inhomogeneity was more obvious. Meanwhile, the texture components began to showcase the deformed $\langle 10\bar{1}0 \rangle$ //ED fiber texture component, which was gradually intensified as the extrusion temperature decreased and became dominant for the temperatures lower than 150 °C.

Grain refinement strengthening and strain hardening

For polycrystals, the grain size d strongly affects the yield strength σ_Y and strain hardening rate, as described by the Hall–Petch relationship [40], $\sigma_{0.2} = \sigma_0 + kd^{-1/2}$, where σ_0 is crystalline friction stress containing the influence of the solute and precipitation, and k is the intrinsic constant of the material. Figure 15 exhibits the relationship between the yield strength $\sigma_{0.2}$ and grain size of the extruded Mg–Nd–Zn–Zr alloys fitted by the Hall–Petch relationship. As shown in Fig. 15a, the Hall–Petch fitted lines differed with the extrusion ratio. At an extrusion ratio of 16, for the stable inclined $\{0002\}$ texture

component extruded at 500–250 °C, the yield stress fitted linearly with the Hall–Petch relationship with the crystalline friction stress σ_0 and slope k determined to be 43.1 MPa and 274.8 MPa $\cdot\mu\text{m}^{1/2}$, which coincided with the literature reports [41]. At an extrusion ratio of 10, for the extrusion temperature varying from 500 to 250 °C, the fitted slope was as high as 689.3 MPa $\cdot\mu\text{m}^{1/2}$ and the σ_0 value was negative. This apparently untrue Hall–Petch relationship stemming from the combined effect of the texture state shifted from the inclined $\{0002\}$ texture at 500 °C to the dispersed fiber texture at 250 °C, along with a large number of deformed grains, at an extrusion ratio of 10. At an extrusion temperature of 150 °C, for both extrusion ratios of 16 and 10, the experimental yield strength values were higher than the values observed from the curve.

The previous studies have shown that the Hall–Petch slope is directly dependent on the texture state and increases with the basal texture strengthening for the slope ranging between 100 and 300 MPa $\cdot\mu\text{m}^{1/2}$ [42, 43]. The texture influenced Hall–Petch relationship could be modified as $\sigma_{0.2} = M(\tau_0 + \kappa d^{-1/2})$, where M is the Taylor factor, and τ_0 is the friction shear stress. The Hall–Petch slope k is positively correlated to the Taylor factor as $k = M\kappa$. Considering the Burger’s vectors in different slip systems, the

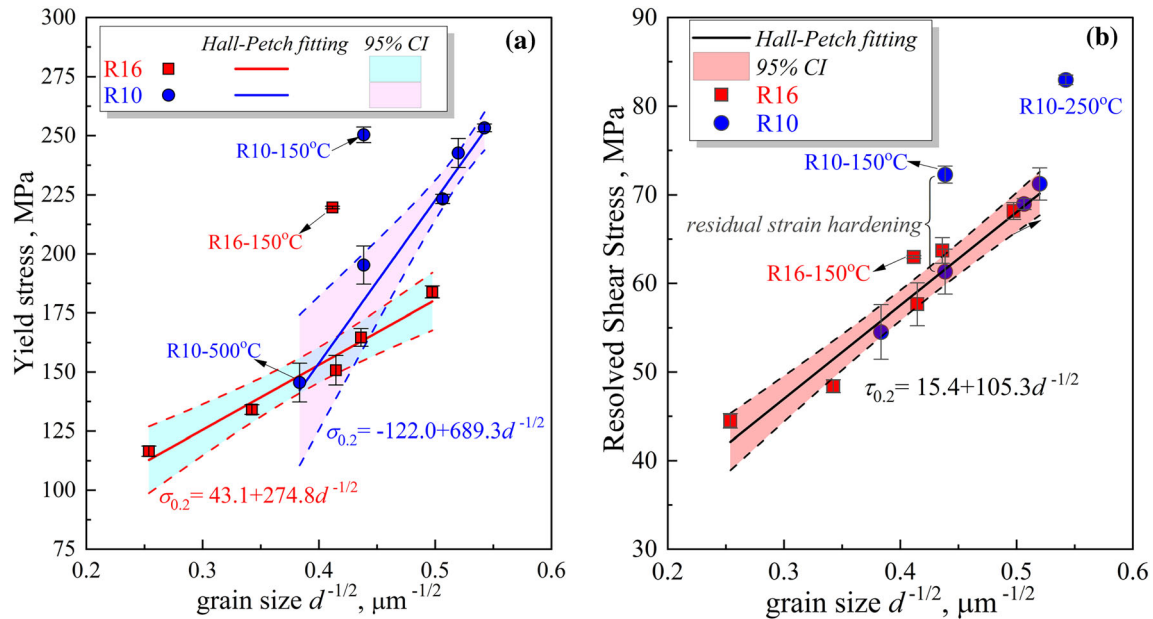


Figure 15 The relationship between **a** yield strength, $\sigma_{0.2}$, and the reciprocal of grain size square root, $d^{-1/2}$, **b** Resolved shear stress and the reciprocal of grain size square root, $d^{-1/2}$.

friction shear stress τ_0 varies, and the strain hardening rate of the different slip systems differs with the dislocation multiplication. Accordingly, it is difficult to characterize the texture influence by solving the Taylor factor with $M = \sum_s \|\dot{\gamma}_s\|/\bar{\epsilon}$ [44] for the magnesium alloys. Therefore, assuming only one slip system in each grain at yield point, the average effective Schmid factor can be calculated as $\bar{m}_{\text{bas}} =$

$$\frac{\tau_{0,\text{bas}}}{\sum_g \sum_s (w_s^g \tau_{0,s} / m_s^g)} \approx 1/\bar{M} \text{ with reference to } \tau_{0,\text{bas}} \text{ of the}$$

basal slip to represent the texture influence, where m_s^g is the Schmid factor in the grain with an operating slip system s , and w_s^g is the corresponding area fraction (equals 0 when not operating and $\sum_g \sum_s w_s^g = 1$).

In order to resolve \bar{M} , the CRSS ratios between the operating systems were required first. Koike et al. [45] estimated $\tau_{0,\text{pris}}/\tau_{0,\text{bas}}$ between 1.5 and 2.0 based on the room temperature tensile analysis. Luo et al. [46] concluded that the slip/twinning CRSS ratio to be between 0.5 and 4.5 for the rolled AZ31B magnesium sheet based on the experiments and calculations. Based on this, the CRSS ratios were selected as basal: twinning: prismatic: pyramidal $\langle c + a \rangle = 1:2:4:2$. With the resolved \bar{M} and $\tau_{0.2} = \frac{\sigma_{0.2}}{\bar{M}} = \tau_{0,\text{bas}} + \kappa d^{-1/2}$, the values of $\tau_{0,\text{bas}} = 15.4$ MPa and

$\kappa = 105.3 \text{ MPa} \cdot \mu\text{m}^{1/2}$ were obtained. On this basis, the fitted line in Fig. 15b was obtained, and the estimated yield strengths on the line agreed well with the experimental results. Meanwhile, $\tau_{0,\text{bas}}$ has been reported to be in the range 12–23 MPa by Wang [47] and Baczmański [48]. It showed that the grain refinement could effectively strengthen the CRSS ratio of the slip systems, and the texture influence took effect by adjusting the macro-stress on the micro-crystalline slip/twinning system at the yield point. The influencing outcome could be estimated by the average effective Schmid factor, \bar{m}_{bas} . Besides, the strain hardening induced by the low temperature raised the $\tau_{0,\text{bas}}$ value at yielding. For instance, an improvement of 12 MPa was observed at an extrusion ratio of 10 and an extrusion temperature of 150 °C. This indicated that the moderate strain hardening at low temperatures could exert a favorable strength improvement, which forms the basis for the strengthening and toughening modification as well as fabrication of the high ductility heat-resistant magnesium alloys.

Ductility improvement and its mechanism

Grain refinement and texture weakening are considered to be the most effective ways to improve the

formability in the magnesium alloys. This study aimed at obtaining the heat-resistant magnesium alloys with an optimal ductility by plastic deformation so as to provide a technique for the fabrication of the high-strength heat-resistant magnesium alloys. The high-ductility heat-resistant Mg–Nd–Zn–Zr alloys rods with an average grain size of 3–8 μm were acquired, and the fracture elongation could be stabilized at 30–40% by the single hot extrusion cycle. In our previous study on the ZK61 magnesium alloys, an improvement in the fracture elongation stemmed from the improved uniform elongation and post-uniform elongation [49]. Specifically, the texture state directly determined the uniform elongation. With the weakening of the basal texture, the uniform elongation increased continuously, and the grain size was responsible for the post-uniform elongation after necking.

Based on this, the relationship between the grain size and fracture elongation is presented in Fig. 16. Apparently, the grain refinement did not lead to an obvious enhancement in the fracture elongation. Instead, a monotonous decline in the elongation was

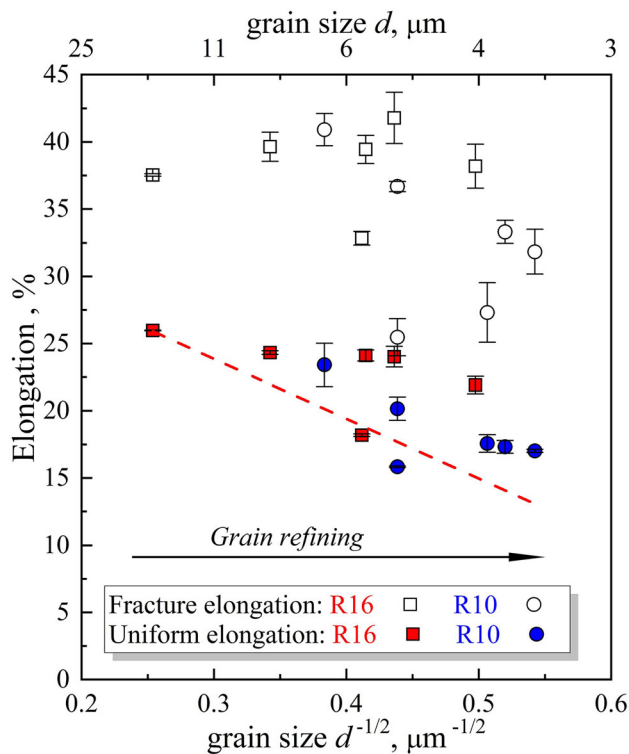


Figure 16 The relationship between the reciprocal of grain size square root, $d^{-1/2}$ and fracture elongation.

observed. However, the grain refinement led to an increase in the post-uniform elongation at the coarse grain region. However, at the fine grain region, the refinement effect on the post-uniform elongation was trivial. In contrast, the ductility improvement in this study mainly resulted from the uniform elongation enhancement affected by the texture state. Compared with the strain hardening behavior, the texture dependence on the uniform elongation was similar to the texture dependence on the room temperature strain hardening behavior, in which the hardening rate was associated with the reciprocal of the basal Schmid factor \bar{m}_{bas} . Likewise, the uniform elongation was linearly related to the Schmid factors. The linear fitting curve of the relationship between the Schmid factor \bar{m}_{bas} and uniform strain ϵ_u is presented in Fig. 17. The linear fitting equation was $\epsilon_u = \alpha + \beta\bar{m}_{bas}$ ($\alpha = 0.10, \beta = 0.86$), which could accurately describe the relationship between the uniform strain and texture state within the data range in this study. However, as \bar{m}_{bas} approached 0, there still existed a high ductility value of 0.1, which was inconsistent with our previous findings for the fine-grained AZ31 wire with a uniform strain less than 0.03 [50]. Therefore, to accurately express the influence of texture on the

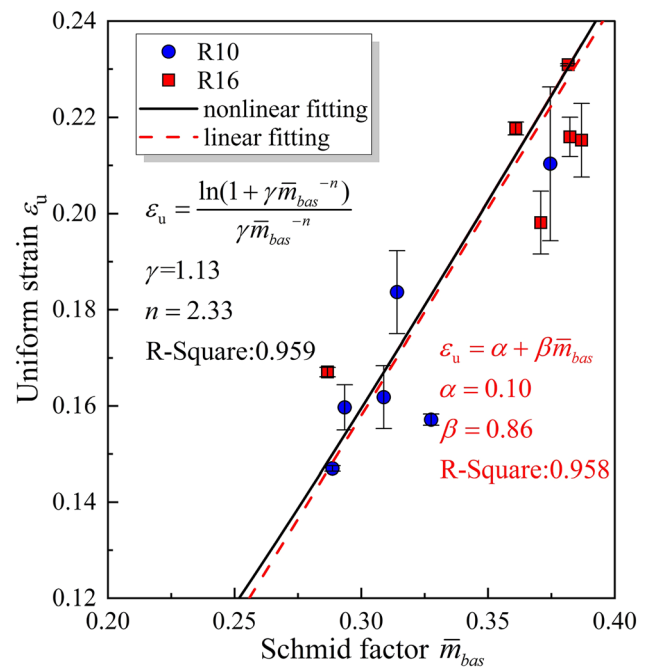


Figure 17 The linear fitting curve of the relationship between Schmid factor and uniform strain.

uniform elongation, Voce hardening equation $\tau - \tau_0 = \tau_1 \left[1 - \exp\left(-\Gamma \frac{\theta_0}{\tau_1}\right) \right]$ was adopted [46], where τ_0 is the resolved shear stress, $\Gamma = \sum_s |\gamma_s|$ is the accumulated slip shear strain, and τ_1 and θ_0 are the constants associated with the material and temperature. Other than the relationship $\bar{m}_{\text{bas}} \approx 1/\bar{M}$ at yielding, as the strain hardening continued, \bar{m}_{bas} gradually decreased, and \bar{M} accordingly increased gradually. Hence, for accuracy, $\bar{M} = \frac{\Gamma}{\varepsilon} = \frac{\sigma - \sigma_0}{\tau - \tau_0} \approx \bar{m}_{\text{bas}}^{-n}$ (\bar{m}_{bas} selected at the start of yielding, $n > 1$) was utilized to transform the macro-stress strain into the slip shear stress and shear strain. The Considère criterion, $d \ln \sigma / d \varepsilon = 1$, was employed to approximately conduct the relationship between the uniform strain ε_u and \bar{m}_{bas} as $\varepsilon_u = \frac{\ln(\lambda \bar{m}_{\text{bas}}^{-n} + 1)}{\lambda \bar{m}_{\text{bas}}^{-n}}$, where $\lambda = \frac{\theta_0}{\tau_1}$ is a constant. Fitting the equation led to $\lambda = 1.13$ and $n = 2.33$. The fitting accuracy was higher than the linear fitting, with ε_u approximated to 0 when \bar{m}_{bas} was 0. In summary, for the high ductility heat-resistant Mg–Nd–Zn–Zr alloy rods, for the grain size less than 8 μm , the ductility improvement was mainly caused by the uniform elongation increment and could be well predicted by the effective Schmid factor \bar{m}_{bas} , which further addressed the importance of the texture modification for the plastic formability of the magnesium alloys.

Conclusion

Aiming at the need for the ductility improvement of the rare-earth magnesium alloys, the influence of the extrusion temperature and extrusion ratio on the microstructure of the Mg–Nd–Zn–Zr alloy rods was analyzed by employing the solution-extrusion technique. The quantitative analysis of the effect of the grain refinement and texture change on the strength and ductility improvement was performed. It was revealed that the texture modification was of significant importance to the strength and ductility improvement. The main conclusions obtained from the study are as follows:

(1) At a solution temperature of 500 °C, the Mg₁₂-Nd grain boundary phase remained after a solution treatment duration of 6 h. The phase completely solubilized in the matrix with the

round Zr precipitation area emerging after 9–18 h. After 24 h, the supersaturated α -Nd segregation was observed. For the extrusion temperature varying within 500–150 °C, predominant dynamic recrystallization and basal texture component transition occurred, leading to the fine-grained microstructure below 300 °C. The heat-resistant magnesium alloy rods with room temperature fracture elongation of 25–40% and yield strength of 181–250 MPa were obtained, which confirmed the ductility modification by the plastic processing method.

- (2) The microstructural evolution in the extrusion process was as follows: as the extrusion process proceeded, a typical <10–10> // ED fiber texture was gradually formed. As the distortion energy accumulated to a certain extent, a discontinuous dynamic recrystallization occurred, which severely refined the microstructure. The orientation of the recrystallized grains was deviated, leading to the weakening of the matrix grains. At the later extrusion stage, the deviated recrystallized grains preferentially grew, and the texture turned into the recrystallized inclined {0002} basal texture. Eventually, the microstructure resulted due to the combined effect of the plastic deformation and dynamic recrystallization.
- (3) The yield strength varied with the extrusion parameters by inducing the microstructure refinement, texture change, or residual strain hardening. The yield strength decreased with the basal texture weakening and could be predicted by the texture influenced Hall–Petch relationship $\frac{\sigma_{0.2}}{\bar{M}} = \tau_{0.2} = \tau_{0,\text{bas}} + \kappa d^{-1/2}$, where, the effective critical shear stress of the dominating slip $\tau_{0,\text{bas}}$ was 15.4 MPa, and the slope κ was 105.3 MPa· $\mu\text{m}^{1/2}$. The texture state \bar{M} could be represented by the reciprocal of the effective Schmid factor \bar{m}_{bas} . The strain hardening induced during the low temperature extrusion could exert an optimal strengthening effect by increasing $\tau_{0,\text{bas}}$ and lowering \bar{m}_{bas} at the yield point.
- (4) The high ductility at the room temperature was determined by the grain refinement and inclined basal texture after extrusion. The grain refinement mainly improved the ductility by increasing the post-uniform elongation;

however, the effect was not obvious in the fine-grained microstructure interfered by the residual strains. In this study, the ductility improvement chiefly resulted from the uniform elongation increment owing to the basal texture weakening, inclined to the orientation perpendicular to the extrusion direction. The uniform strain could be estimated with the initial effective Schmid factor $\overline{m}_{\text{bas}}$ at yielding by using the equation: $\varepsilon_{\text{u}} = \frac{\ln(\lambda \overline{m}_{\text{bas}}^{-n} + 1)}{\lambda \overline{m}_{\text{bas}}^{-n}}$.

Acknowledgements

This work was supported by National Natural Science Foundation of China (Grant No. 51975146), Shandong Province Natural Science Foundation (Grant No. ZR2020QE171), Key Technology Research and Development Program in Shandong Province (Grant Nos. 2019JZZY010364, 2018JMRH0412), and National Defense Basic Scientific Research Program of China (Grant No. JCK2018603C017)

References

- Wang SH, Zhang WC, Wang HX, Yang JL, Chen WZ, Cui GR, Wang GF (2021) Microstructures evolution, texture characteristics and mechanical properties of Mg–2.5Nd–0.5Zn–0.5Zr alloy during the high strain rate hot-rolling. *Mater Sci Eng A* 803:140488. <https://doi.org/10.1016/j.msea.2020.140488>
- Xia X, Zhang K, Ma M, Li T (2020) Constitutive modeling of flow behavior and processing maps of Mg–8.1 Gd–4.5Y–0.3Zr alloy. *J Magnes Alloy* 8(3):917–928
- Yin DD, Wang QD, Gao Y, Chen CJ, Zheng J (2011) Effects of heat treatments on microstructure and mechanical properties of Mg–11Y–5Gd–2Zn–0.5Zr (wt.%) alloy. *J Alloy Compd* 509(5):1696–1704
- Pan FS, Yang MB, Chen XH (2016) A review on casting magnesium alloys: modification of commercial alloys and development of new alloys. *J Mater Sci Technol* 32(12):1211–1221
- Wang J, Meng J, Zhang D, Tang D (2007) Effect of Y for enhanced age hardening response and mechanical properties of Mg–Gd–Y–Zr alloys. *Mater Sci Eng A* 456(1–2):78–84
- Liu XB, Chen RS, Han EH (2008) Effects of ageing treatment on microstructures and properties of Mg–Gd–Y–Zr alloys with and without Zn additions. *J Alloy Compd* 465(1–2):232–238
- Rong W, Zhang Y, Wu YJ, Chen YL, Sun M, Chen J, Peng LM (2019) The role of bimodal-grained structure in strengthening tensile strength and decreasing yield asymmetry of Mg–Gd–Zn–Zr alloys. *Mater Sci Eng A* 740:262–273
- Gui ZZ, Kang ZX, Li YY (2019) Mechanical and corrosion properties of Mg–Gd–Zn–Zr–Mn biodegradable alloy by hot extrusion. *J Alloy Compd* 685:222–230
- Zhang HH, Fan JF, Zhang L, Wu GH, Liu WC, Cui WD, Feng S (2016) Effect of heat treatment on microstructure, mechanical properties and fracture behaviors of sand-cast Mg–4Y–3Nd–1Gd–0.2Zn–0.5Zr alloy. *Mater Sci Eng A* 677:411–420
- Zhang Z, Liu X, Wang Z, Le Q, Hu W, Bao L, Cui J (2015) Effects of phase composition and content on the microstructures and mechanical properties of high strength Mg–Y–Zn–Zr alloys. *Mater Des* 88:915–923
- Tan X, Chee KHW, Chan KWJ, Richard WO, Kwok MG (2015) Effect of homogenization on enhancing the failure strain of high strength quaternary LPSO Mg–Y–Zn–Al alloy. *Mater Sci Eng A* 644:405–412
- Rong W, Wu Y, Zhang Y, Sun M, Chen J, Peng L, Ding W (2017) Characterization and strengthening effects of γ' precipitates in a high-strength casting Mg–15Gd–1Zn–0.4Zr (wt.%) alloy. *Mater Charact* 126:1–9
- Zhang Y, Wu Y, Peng L, Fu P, Huang F, Ding W (2014) Microstructure evolution and mechanical properties of an ultra-high strength casting Mg–15.6Gd–1.8Ag–0.4Zr alloy. *J Alloy Compd* 615:703–711
- Zhang Q, Li QN, Jing XT, Zhang XY (2010) Microstructure and mechanical properties of Mg–10Y–2.5Sm alloy. *J Rare Earth* 28:375–377
- Yu ZJ, Xu C, Meng J, Zhang XH, Kamado S (2017) Effects of pre-annealing on microstructure and mechanical properties of as-extruded Mg–Gd–Y–Zn–Zr alloy. *J Alloy Compd* 729:627–637
- Qi F, Zhang D, Zhang X, Xu X (2014) Effects of Mn addition and X-phase on the microstructure and mechanical properties of high-strength Mg–Zn–Y–Mn alloys. *Mater Sci Eng A* 593:70–78
- Zhao SC, Guo EJ, Cao GJ, Wang LP, Lun YC, Feng YC (2017) Microstructure and mechanical properties of Mg–Nd–Zn–Zr alloy processed by integrated extrusion and equal channel angular pressing. *J Alloy Compd* 705:118–125
- Zhang D, Yang Q, Zhang D, Guan K, Bu F, Zhou H, Meng J (2017) Effects of substitution of Nd in a sand-cast Mg–2.5Nd–0.6Zn–0.5Zr alloy with x wt.% Sm (x = 2.5, 4, and 6). *J Rare Earth* 35(12):1261–1267

- [19] Wu D, Chen RS, Ke W (2014) Microstructure and mechanical properties of a sand-cast Mg-Nd-Zn alloy. *Mater Des* 58:324–331
- [20] Guan K, Yang Q, Bu FQ, Qiu X, Sun W, Zhang DP, Zheng T, Niu XD, Liu XJ, Meng J (2017) Microstructures and mechanical properties of a high-strength Mg–3.5Sm–0.6Zn–0.5Zr alloy. *Mater Sci Eng A* 703:97–107
- [21] Bohlen J, Nürnberg MR, Senn JW, Letzig D, Agnew SR (2007) The texture and anisotropy of magnesium-zinc-rare earth alloy sheets. *Acta Mater* 55:2101–2112
- [22] Okamoto H (1991) Mg-Nd (Magnesium-Neodymium). *J Phase Equilib* 12(2):249–250
- [23] Wang WZ, Wu D, Chen RS, Qi Y, Ye HQ, Yang ZQ (2020) Revisiting the role of Zr micro-alloying in a Mg–Nd–Zn alloy. *J Alloy Compd* 832:155016. <https://doi.org/10.1016/j.jallcom.2020.155016>
- [24] Zhou YY, Fu PH, Peng LM, Wang D, Wang YX, Hu B, Liu M, Sachdev AK, Ding WJ (2019) Precipitation modification in cast Mg–1Nd–1Ce–Zr alloy by Zn addition. *J Magnes Alloy* 7(1):113–123
- [25] Gavras S, Subroto T, Buzolin RH, Hort N, Tolnai D (2018) The role of Zn additions on the microstructure and mechanical properties of Mg–Nd–Zn alloys. *Int J Metalcast* 12(3):428–433
- [26] Zheng XW, Dong J, Wang SM (2018) Microstructure and mechanical properties of Mg–Nd–Zn–Zr billet prepared by direct chill casting. *J Magnes Alloy* 6(1):95–99
- [27] Ha C, Bohlen J, Zhou X, Brokmeier HG, Kainer KU, Schell N, Letzig D, Yi S (2021) Texture development and dislocation activities in Mg–Nd and Mg–Ca alloy sheets. *Mater Charact* 175:111044. <https://doi.org/10.1016/j.matchar.2021.111044>
- [28] Fu PH, Peng LM, Jiang HY, Zhai CQ, Gao X, Nie JF (2007) Zr-containing precipitates in Mg–3wt%Nd–0.2wt%Zn–0.4wt%Zr alloy during solution treatment at 540 °C. *Mater Sci Forum* 546–549:97–100
- [29] Yu ZJ, Xu C, Meng J, Liu K, Fu JL, Kamado S (2019) Effects of extrusion ratio and temperature on the mechanical properties and microstructure of as-extruded Mg–Gd–Y–(Nd/Zn)–Zr alloys. *Mater Sci Eng A* 762:138080. <https://doi.org/10.1016/j.msea.2019.138080>
- [30] Zhao T, Hu Y, Zhang C, He B, Zheng T, Tang A, Pan F (2020) Influence of extrusion conditions on microstructure and mechanical properties of Mg–2Gd–0.3Zr magnesium alloy. *J Magnes Alloy*. <https://doi.org/10.1016/j.jma.2020.06.019>
- [31] Guo KK, Liu MY, Wang JF, Sun YF, Li WQ, Zhu SJ, Wang LG, Guan SK (2020) Microstructure and texture evolution of fine-grained Mg–Zn–Y–Nd alloy micro-tubes for biodegradable vascular stents processed by hot extrusion and rapid cooling. *J Magnes Alloy* 8(3):873–882
- [32] Zhang L, Chen W, Zhang W, Wang W, Wang E (2016) Microstructure and mechanical properties of thin ZK61 magnesium alloy sheets by extrusion and multi-pass rolling with lowered temperature. *J Mater Process Technol* 237:65–74
- [33] Cui C, Zhang W, Chen W, He J, Chen X, Hou J (2021) Microstructure, texture evolution and yield strength symmetry improvement of as-extruded ZK60 Mg alloy via multi-directional impact forging. *J Magnes Alloy*. <https://doi.org/10.1016/j.jma.2021.01.001>
- [34] Chen WZ, Wang X, Hu LX, Wang E (2012) Fabrication of ZK60 magnesium alloy thin sheets with improved ductility by cold rolling and annealing treatment. *Mater Des* 40:319–323
- [35] Humphreys FJ, Hatherly M (2012) Recrystallization and related annealing phenomena. Elsevier, Oxford, p 250
- [36] Cano-Castillo G, Victoria-Hernández J, Bohlen J, Letzig D, Kainer KU (2020) Effect of Ca and Nd on the microstructural development during dynamic and static recrystallization of indirectly extruded Mg–Zn based alloys. *Mater Sci Eng A* 793:139527. <https://doi.org/10.1016/j.msea.2020.139527>
- [37] Mayama T, Noda M, Chiba R, Kuroda M (2011) Crystal plasticity analysis of texture development in magnesium alloy during extrusion. *Int J Plast* 27:1916–1935
- [38] Wang WK, Chen WZ, Zhang WC, Cui GR, Wang ED (2018) Effect of deformation temperature on texture and mechanical properties of ZK60 magnesium alloy sheet rolled by multi-pass lowered-temperature rolling. *Mater Sci Eng A* 712:608–615
- [39] Meza-García E, Bohlen J, Yi S, Letzig D, Kräusel V, Landgrebe D, Kainer KU (2015) Influence of alloying elements and extrusion process parameter on the recrystallization process of Mg–Zn alloys. *Mater Today Proc* 2:S19–S25
- [40] Hall E (1951) The deformation and ageing of mild steel: III discussion of results. *Proc Phys Soc Section B* 64(9):747–753
- [41] Jain A, Duygulu O, Brown DW, Tome CN, Agnew SR (2008) Grain size effects on the tensile properties and deformation mechanisms of a magnesium alloy, AZ31B, sheet. *Mater Sci Eng A* 486(1–2):545–555
- [42] Yuan W, Panigrahi SK, Su JQ, Mishra RS (2011) Influence of grain size and texture on Hall–Petch relationship for a magnesium alloy. *Scr Mater* 65(11):994–997
- [43] Chen WZ, Wang X, Kyalo MN, Wang ED, Liu ZY (2013) Yield strength behavior for rolled magnesium alloy sheets with texture variation. *Mater Sci Eng A* 580:77–82
- [44] Sahoo SK, Toth LS, Biswas S (2019) An analytical model to predict strain-hardening behaviour and twin volume fraction in a profoundly twinning magnesium alloy. *Int J Plast* 119:273–290
- [45] Koike J, Kobayashi T, Mukai T, Watanabe H, Suzuki M, Maruyama K, Higashi K (2003) The activity of non-basal slip systems and dynamic recovery at room temperature in

- fine-grained AZ31B magnesium alloys. *Acta Mater* 51(7):2055–2065
- [46] Lou XY, Li M, Boger RK, Agnew SR, Wagoner RH (2007) Hardening evolution of AZ31B Mg sheet. *Int J Plast* 23(1):44–86
- [47] Wang LY, Huang ZH, Wang HM, Maldar A, Yi SB, Park JS, Kenesei P, Lilleodden E, Zeng XQ (2018) Study of slip activity in a Mg-Y alloy by in situ high energy X-ray diffraction microscopy and elastic viscoplastic self-consistent modeling. *Acta Mater* 155:138–152
- [48] Baczmanski A, Wronski M, Kot P, Wronski S, Labaza A, Wierzbanski K, Ludwik A, Marciszko-Wiackowska M (2021) The role of basal slip in the generation of intergranular stresses in magnesium alloy studied using X-ray diffraction and modelling. *Mater Des* 202:109543. <https://doi.org/10.1016/j.matdes.2021.109543>
- [49] Chen WZ, Wang X, Wang ED, Liu ZY, Hu LX (2012) Texture dependence of uniform elongation for a magnesium alloy. *Scr Mater* 67(10):858–861
- [50] Chen WZ, Zhang WC, Chao HY, Zhang LX, Wang ED (2015) Influence of large cold strain on the microstructural evolution for a magnesium alloy subjected to multi-pass cold drawing. *Mater Sci Eng A* 623:92–96

Publisher's Note Springer Nature remains neutral with regard to jurisdictional claims in published maps and institutional affiliations.